Korean J. Chem. Eng., 40(9), 2303-2311 (2023)
DOI: 10.1007/s11814-023-1421-3

pISSN: 0256-1115
eISSN: 1975-7220

Designing CuSe-gCN nanocomposite as an active electrocatalyst for water oxidation

Fatemah Farraj Alharbi*, Zahoor Ahmad, Adeel Hussain Chughtai***, Rabia Yasmin Khosa****, and Hafiz Muhammad Tahir Farid*****,†**

*Department of Physics, College of Science, Princess Nourah bint Abdulrahman University, P.O. Box 84428, Riyadh 11671, Saudi Arabia
**Department of Physics, University of Engineering Lahore, Pakistan
***Institute of Chemical Sciences, Bahauddin Zakariya University, Multan-60800, Pakistan
****University of Education, Lahore, Dera Ghazi Khan Campus, D. G. Khan 32200, Pakistan
*****Department of Physics, Government college Taunsa Sharif- 32200, Pakistan
(*Received 23 December 2022 • Revised 13 February 2023 • Accepted 17 February 2023*)

Abstract−CuSe-gCN nanocrystals were premeditated and produced utilizing a simple hydrothermal method. Different analytical techniques well characterized the generated samples. The prepared samples also contain nanocrystals with a vertical shape, decorated with numerous nanoparticles. All characterizations confirm the phase composition of composite CuSe-gCN. The pore size of the N_2 adsorption-desorption isotherm also pointed to a mesoporous structure. Furthermore, the combination of distinct morphology nanoparticles embellished on gCN graphitized nanotubes helps to achieve larger current densities and lower starting potentials for the oxygen evolution process. Because of their unique mesoporous structure, the CuSe-gCN catalysts show exceptional electrical conductivity and electrocatalytic activity. Compared to monometallic CuSe and gCN, CuSe-gCN significantly lower overpotential of 208 mV was needed to obtain a current density of 10 mA/cm^2. The CuSe-gCN nanocrystals displayed good stability and a low Tafel slope of 35 mV/dec. This research shows that it is possible to use a copper-based selenide with gCN and combine all the beneficial characteristics in a single catalyst system.. Still, it also offers fresh perspectives on the logical proposal and creation of effective electrocatalysts for various applications.

Keywords: CuSe/gCN, Electrocatalyst, Hydrothermal Process, Alkaline Media, Water Splitting

INTRODUCTION

The pressing necessity for diverse situations to get energy is caused by the rapid depletion of fossil resources [1-6]. There has been much research interest in creating alternative techniques for efficiently utilizing sustainable renewable energy worldwide [7-10]. Finding new energy sources with realistic potential for delivering useful energy is one of the biggest difficulties, say experts [11-15]. Making sustainable energy using electrochemical water splitting is a simple and inexpensive technology that might one day replace fossil fuels [16-18]. Another vital route for grid-scale energy storage is energy conversion, which involves converting renewable energy into various chemical energies [18]. Separating water into its component parts and using photon energy to produce chemical energy is one practical way to address the current energy dilemma [19].

The progress of electrolysis by imitating nature's method has turned into a crucial path for a society, constructed on renewable and sustainable energy [20-24]. Water electrolysis, which involves the anodic oxygen evolution reaction (OER) and the cathodic hydrogen evolution reaction (HER), has a high thermodynamic barrier, which makes it very intensive [25-27]. As a result, creating effective dual-functional OER and HER catalysts for overall water splitting continues to be quite tricky and requires much effort [28,29]. Modern electrocatalysts for performing water splitting mostly rely on materials based on noble metals (IrO_2 and RuO_2 for OER and Platinum for HER). However, the small availability of these rare elements restricts their widespread applied use [30-33].

On the other hand, new research suggests that a careful selection of nature-abundant transition-metal (TM) based electrocatalysts, notably the first-row transition metals, could enhance OER catalytic activity [34-37]. It is essential to research low-cost, dependable options with high electrocatalytic activity for water oxidation [38-40]. Science is quite interested in nonprecious metal-based oxides, carbonaceous compounds, and hydroxides [41]. Devi et al. used a chemical deposition technique to produce NiSe/GCN nanocomposites. The said catalyst, whose usual particle size is 20 nm, has the lowest overpotential at 351 mV at 50 mA/cm^2. This is lower than the overpotential of pure $Ni(OH)_2$ nanosheets, which is 371 mV [42]. Hot injection technology was used by Rui Gao et al. to successfully manufacture 2D $FeSe_2$ nanoplatelets, revealing incredibly high catalytic activity and consistency for OER. The exceptional electrocatalytic activity of $FeSe_2$/NF nanoplatelets is due to high-exposure active sites, which needed an overpotential of 380 mV with a 52 mV/dec Tafel slope value and steady current densities after 65 h [43]. On the $MoSe_2$ and $SnSe_2$ heterostructures, the HER and OER are conducted separately. More intriguingly, the selenide vacancy in the $MoSe_2$ monolayer considerably lowers the OER overpotential, allowing the catalytic processes to happen naturally at potentials exclu-

†To whom correspondence should be addressed.
E-mail: tahirfaridbzu@gmail.com

sively supplied by electro-generated electrons in water [44].

Copper is among the most prevalent metals, and copper-based materials and constituents have been extensively used for electrical and electronic devices due to their high catalytic performance and conductivity [45,46]. In addition, copper and its oxide nanoparticles have been utilized as extremely effective catalysts for the reduction of CO_2. Recently, Cu-based nanomaterials have also been used as effective electrocatalysts for OER in a small number of instances. Due to advantageous OER action in alkaline electrolytes, copper pnictides and chalcogenides have attracted much interest in this approach [47-49]. Moreover, A novel family of metal selenides has been termed "star chalcogenides" in a manner similar to this because of the significant advantages it offers over more traditional metal oxides and selenides. Se atoms in the 3d orbital participate in bonding, raising the energy level of the 3s and 3p orbitals and resulting in higher metallicity [50-52]. But trend-tuning strategies, such as morphological design, hybridization, and doping, are said to successfully enhance the material qualities. The selenium addition can modify the catalyst's electronic structure and surface geometry, which can change the catalytic activity [53,54]. Meanwhile, recent research has focused on composites constructed of graphitic carbon nitride (gCN) that act as electrocatalysts for the splitting of water [55,56]. Since simple gCN is nearly imperceptibly slow for OER, the catalytic activity is mostly related to the synergistic interaction of gCN with conductive materials. To develop highly effective electrocatalysis that occurs in an aqueous medium, however, gCN is a desired component due to the several unique physiochemical properties. The high-water aqueous solubility of proton-functionalized gCN nanosheets, which would considerably improve the wettability of materials, including such gCN nanosheets, is an essential point to make [57].

We assume that building CuSe-gCN would significantly increase the catalyst hydrophilicity compared to bare CuSe based on the aforementioned findings. Additionally, the presence of g-gCN is an attractive source with numerous prospective applications across a variety of disciplines due to its unique features and inexpensive price. Its high stability, catalytic activity, and optical features make it a compelling alternative to conventional materials in a range of applications, and its potential for future improvement and development makes it a fascinating study topic. Hence, using gCN would effectively provide good dispersion and prevent CuSe aggregation. Thus, gCNs would enable the CuSe-gCN hybrid to produce very effective and long-lasting chemical oxidation catalysis. In this instance, a simple hydrothermal technique was used to create a gCN hybrid with monodispersed CuSe nanoplates tightly connected with gCN nanosheet responses high conductivity, because comparable to the conductivity of other semiconductors, copper selenide is an excellent electrical conductor. Even though the intrinsic gCN electrocatalytic ability is poor and CuSe has low catalytic activity, still, the hybrid gCN offers meaningly increased electrocatalytic capacity for OER contrasted to naked ultrathin CuSe NPs. The high electrochemical activity proposes that in addition to boosting inherent catalytic performance and revealing more active sites, it is crucial to develop an effective catalyst surface to obtain faster catalytic reaction kinetics. In alkaline media, CuSe-gCN delivers 10 mA/cm^2 current density at 208 mV overpotential with a negligible 35 mV/dec Tafel slope.

EXPERIMENTAL SECTION

1. Chemical Reagent

Copper nitrate hexahydrate (99.8%, $Ce(NO_3)_3{\cdot}6H_2O$, Merck), melamine (98.9%, $C_3H_6N_6$, 99.8%, Emparta), selenium powder (96%, Se, Sigma Aldrich), hexamethylene tetraamine (58%, HMTA, Emsure), potassium hydroxide (KOH, 85.9%, reagent DUKSAN), and ethyl alcohol (97.8%, C_2H_5OH, AnalaR) were all used during synthesis, without being further purified before usage. The deionized water used in the experiment came from a purifier.

2. Synthesis of gCN

Previous findings indicated that graphitic carbon nitride (gCN) was made using melamine [58]. 15.7 g of melamine was heated in an electric furnace for 3 h at 420 °C at a heating rate of 4 °C/min. The recovered gCN was afterward employed in further compounds as a grayish powder.

3. Synthesis of CuSe and CuSe-gCN

To produce CuSe, a straightforward hydrothermal technique was employed, and during a 40-minute period of continuous stirring, (1.802 g) Cu $(NO_3)_3$ and (1.712 g) hexamethylene tetra amine (HMT) were combined with 40 mL DI water and 30 mL C_2H_5OH. The mixture was then put into a Teflon-coated autoclave and kept for 6 hours at 180 °C. The acquired green precursor was cleaned using ethanol and DI H_2O. After that, it was dried for 15 hours at 60 °C. Then, 30 minutes of continuous stirring was performed while adding 60 mL of DI water and 0.467 g of selenium powder. It was next cooked for 12 hours at 140 °C in a hydrothermal autoclave. To create the black-colored CuSe ppts, the following washing and drying steps were repeated.

The production of CuSe-gCN nanocomposites involved only simple mechanical mixing and heating. Then, a homogeneous mixture containing 20.7 mg of produced CuSe solution and 45.7 mg of gCN composites was heated, transferred to 100 ml autoclave, and placed for 6 hours at 210 °C in an oven.

4. Physical Characterization

For chemical bonding and crystallographic investigations, the generated materials were evaluated using an X-ray diffraction (XRD) instrument via (Advance Bruker D8) powder X-ray diffraction machine. The Debye-Scherrer Eq. (1) was castoff to find the size of crystallite from the XRD patterns:

$$D = \frac{k\lambda}{\beta\cos\theta} \quad (1)$$

The morphology of the prepared CeS-g-CN samples has been shown utilizing a scanning electron microscope (Carl Zeiss, EVO 18, SEM, Japan). Using Bruker's Alpha FTIR instrument, Fourier transform infrared (FTIR, ZEISS-Merlin) spectroscopy was used to validate that the manufactured substance's molecules have a particular structure (500-4,000 cm^{-1}). The Brunauer-Emmett-Teller (BET) and Barret-Joyner-Halenda (BJH) techniques were utilized to examine surface characteristics using the Micromeritics ASAP 2020 system.

5. Chemical Characterization

In a three-electrode arrangement, a potentiostat (Ivium Stat) was used to measure the electrocatalytic activity of CuSe/PPy in a 1 M

solution of KOH. The working electrode was CuSe/PPy drop-cast on Ni-form substrates for all electrochemical studies. This allowed us to study the OER catalytic activities. The potentials of the catalyst were referenced to a reversible hydrogen electrode (RHE):

$$E_{RHE} = E_{Ag/Agcl} + 0.059 \times pH + E_0 \quad (2)$$

The overpotential was calculated through this formula:

$$\eta = E_{RHE} - 1.23 \quad (3)$$

Tafel plots were created by redrawing the polarization curve as the overpotential to the logarithm of current density, and the linear portion was calculated by utilizing the Tafel equation:

$$\eta = b\log|j| + a \quad (4)$$

To assess the prepared catalysts' performance was determined in the range of potential window (0-2.0 V). To determine the actual electrochemical active surface area, electrochemical capacitance characteristics were examined by CV at various scan rates. Measurements of (C_{dl}) double-layer capacitance were used to calculate the ECSA could be calculated using the formula:

$$C_{dl} = \frac{\text{Slope}}{2} \quad (5)$$

$$\text{ECSA} = \frac{C_{dl}}{C_{sp}} \quad (6)$$

A conventional three-electrode arrangement was employed for the electrochemical impedance spectroscopy (EIS) testing. The catalyst with a Ni-foam was used as the working electrode without additional processing. Platinum foil served as the counter electrode. KOH in an argon-saturated 1.0 M solution served as an electrolyte. The Ag/AgCl saturated electrode was utilized as the reference electrode with a 10 mV/s scan rate. EIS was executed at frequencies ranging from 100 kHz-0.1 Hz. Every cyclic voltammetry curve underwent an IR correction (50%). The following equation was utilized for manually compensating potential values.

$$E_{actual} = E_{experimental} - IR \quad (7)$$

Chronoamperometry was employed to measure the stability and durability of the electrocatalysts throughout time periods of 1 and 100 h at the constant applied potential.

RESULTS AND DISCUSSION

CuSe-gCN, CuSe, and gCN were all synthesized in primary conditions using a straightforward hydrothermal method. Fig. 1 demonstrates that the fabrication of CuSe-gCN was successful by showing the typical XRD patterns of CuSe, gCN, and CuSe-gCN in their as-prepared states. At 26°, a small peak of gCN was present. Also, other diffraction peaks at 31°, 45.9°, 53°, 60.3°, 66° and 73.9°, respectively, can be ascribed to the (0 0 6), (1 0 7), (2 0 1), (1 1 10), (2 0 7), and (2 1 1) h k l planes of hexagonal CuSe-gCN ($JCPD_S$ No. 00-034-0171) based on the XRD pattern [59]. No extra diffraction peaks were visible in the XRD patterns. Additionally, the extensive experimental results demonstrate that the molar ratio of CuSe, or more specifically, the reactant quantities, has a considerable influence on

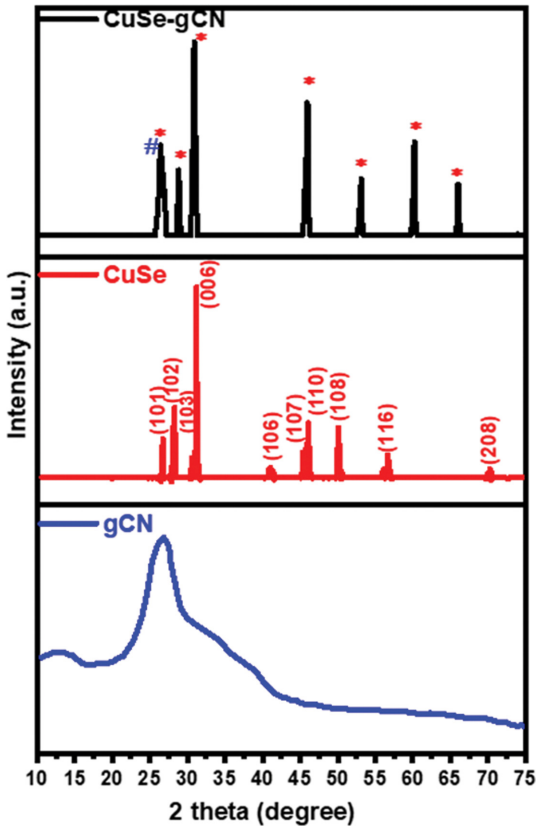

Fig. 1. Comparison of XRD pattern for CuSe-gCN, CuSe and gCN.

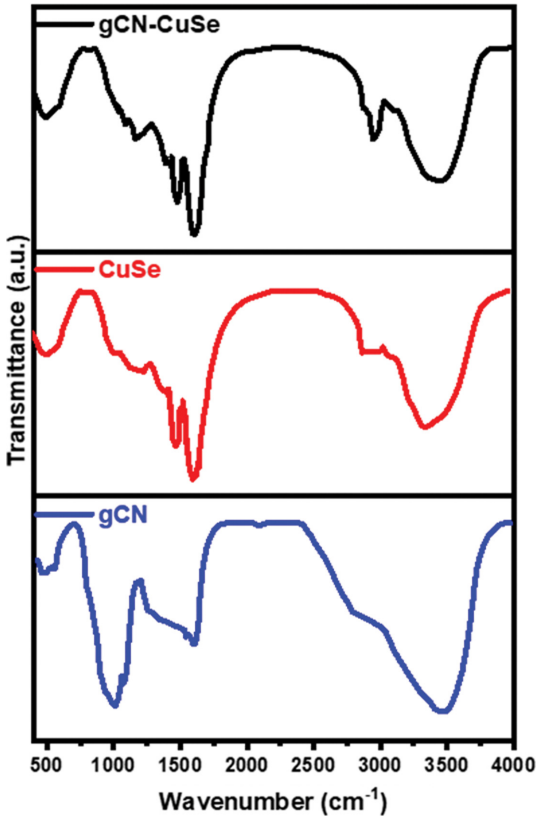

Fig. 2. Comparison of FTIR pattern for CuSe-gCN, CuSe and gCN.

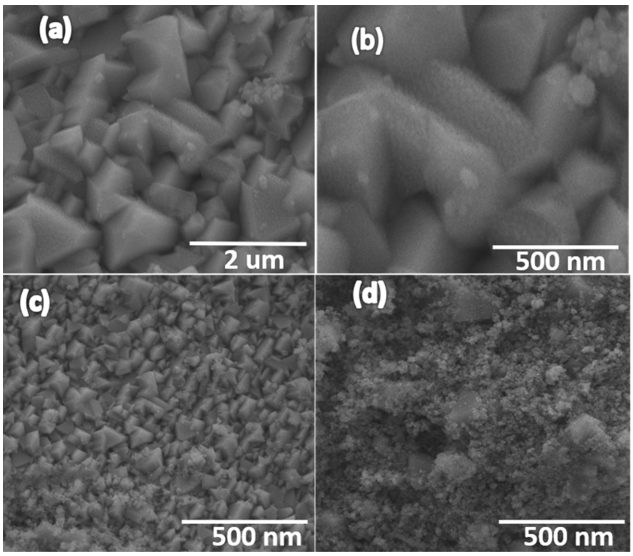

Fig. 3. SEM analysis for (a)-(b) CuSe-gCN, (c) CuSe, and (d) gCN at different magnification power.

the phase composition. The diffraction peaks' broadness indicates the presence of small crystallites, and according to Scherrer's formula, the CuSe, gCN, CuSe-gCN particle's crystallite size is roughly 40 nm, 31.7 nm, and 11 nm, respectively. Due to its small size, it provides a large surface area for reaction.

The FT-IR spectra of CuSe-gCN are shown in Fig. 2. It has been discovered that the CuSe-gCN sample exhibits two broad and wide peaks, one at 620 cm^{-1}, which is assigned to the CuSe band and represents selenide, and the other at 3,452 cm^{-1}, which corresponds to the O-H stretching vibration [60]. The bands from the CuSe-gCN sample's FTIR spectra are well-aligned with the values that have been published. The signal at 1,162 cm^{-1} comes from the triazine ring mode, which agrees to condensed CN heterocycles in g-CN nanosheets. The absorption peak at 2,947, 1,630 cm^{-1} is brought on by the C double bond N stretching of g-CN. g-CN's single bond, double bond, and N stretching, on the other hand, correspond to the absorption peaks at 1,483 cm^{-1}.

Table 1. BET isotherm comparison (a) Specific surface area (b) Pore size of CuSe-gCN (c) CuSe and (d) gCN

Sr. no	Material	BET SSA (m^2/g)	Pore size (nm)
1	CuSe	36.7	6.2
2	gCN	49	4.45
3	CuSe-gCN	66	2.36

The as-synthesized materials' shape and structure were investigated using SEM. CuSe-as-obtained gCN's framework was examined, and it was discovered that it preserved the nanocrystals' architecture when they combined to form nanoclusters (Fig. 3(a), (b)). CuSe-gCN nanocrystals with a vertical shape are decorated with numerous nanoparticles, which not only makes it easier to expose the active sites for surface reactions but also creates spaces for the expulsion of oxygen gas bubbles during ongoing OER activity, which in turn increases OER activity for a more extended period of time [61]. CuSe, in contrast, is composed of tiny crystals with a smooth surface arranged in a beads pattern resembling the structures in Fig. 3(c). CuSe exhibits nanocrystals that resemble beads. Additionally, the morphology of nanosheets with tiny standing nanostructures is seen in the SEM analysis for graphitized carbon nanotubes in Fig. 3(d).

The nitrogen adsorption-desorption isotherm was then found by using the Brunauer-Emmett-Teller (BET) technique to determine the precise surface area and pore size distribution [62]. In Fig. 4(a), the N_2 adsorption-desorption plot for CuSe-gCN corresponds to an IV type isotherm, which raises the possibility of a mesoporous structure. It was further demonstrated that the CuSe-gCN nanocrystals made using the Barrett-Joyner-Halenda (BJH) technique have a mesoporous architecture with a pore size of 2.36 nm (Fig. 4(b)). Additionally, the CuSe-gCN as-built surface area was 66 m^2/g (Fig. 4(a)). Materials are transported more easily because of the mesoporous structure and vast surface area, as tabulated in Table 1.

Using a typical three-electrode setup made up of a working electrode (Nickel foam enclosed with the produced materials), a pt wire served as a counter electrode, and a reference electrode (Ag/AgCl),

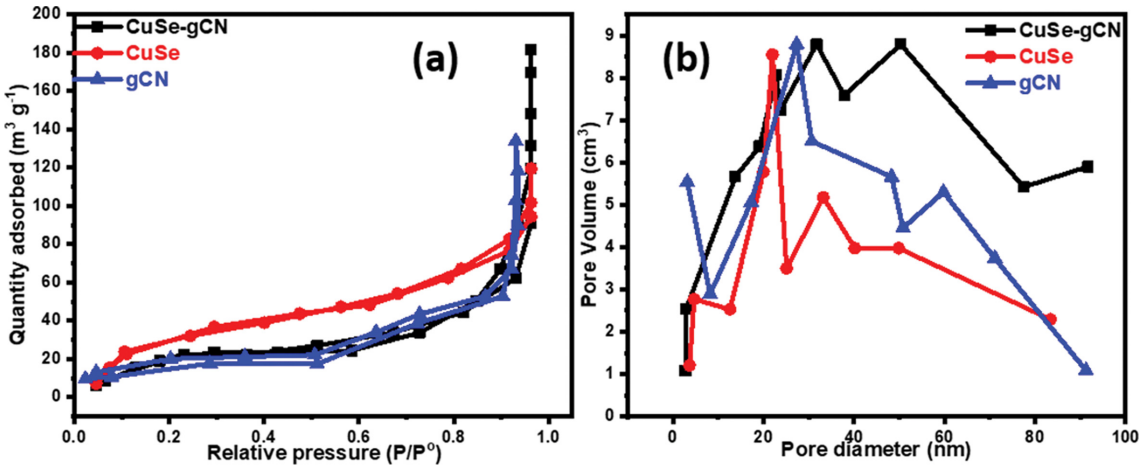

Fig. 4. (a) BET isotherm analysis and (b) Pore size distribution curve analysis of fabricated materials.

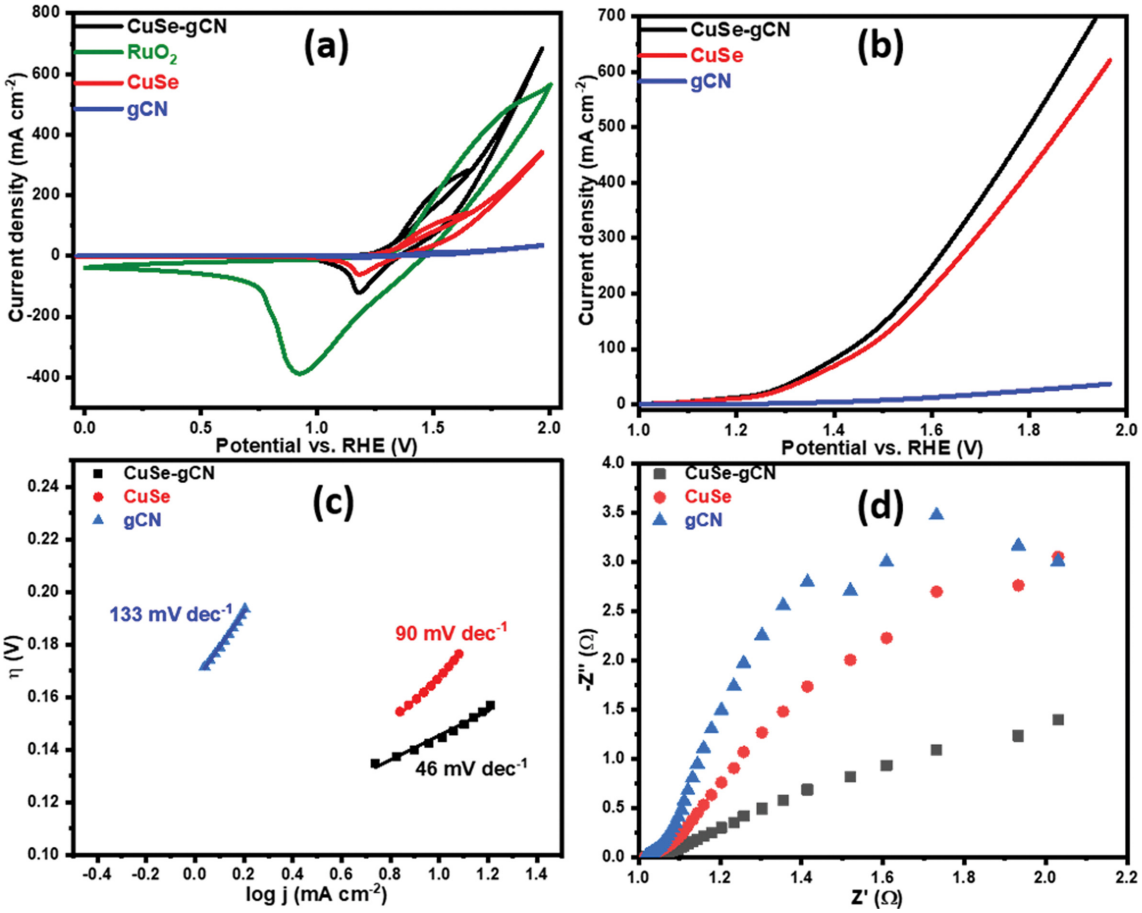

Fig. 5. Comparison of electrochemical activity in 1 M KOH solution (a) CV (b) LSV (c) Tafel analysis (d) Nyquist plot.

the electrochemical properties of each sample were evaluated in basic electrolyte. LSV tests were conducted to evaluate the catalytic performance at a 10 mV/s scan rate. CuSe-gCN nanocrystals, as synthesized, as shown in Fig. 5(a), (b), require the least voltage when compared to the other materials to produce the same current density. More specifically, at a current density of 10 mA/cm^2, the CuSe-gCN (208 mV) catalyst showed a lower overpotential than the comparable CuSe (294 mV), gCN (360 mV) catalysts. The synergistic interaction and peculiar mesoporous structure of the metals may be the cause of CuSe-enhanced gCN's electrocatalytic activity. It was feasible to get insights into the OER kinetics by analyzing the Tafel slopes of various electrocatalysts using Tafel plots based on LSV data, where the horizontal axis corresponds to the overpotential and the vertical coordinate is given to log j. The Tafel slope of the composite CuSe-gCN electrocatalyst is only 35 mV/dec, which is less than that of the pure CuSe (89 mV/dec) and gCN (122 mV/dec) electrocatalysts (Fig. 5(c)). The CuSe-gCN nanocrystals' unusual mesoporous structure may be related to their decreased Tafel slope, which anticipated more effective kinetics and demonstrated a fast rise in current density with increasing overvoltage.

To learn more about the reaction kinetics of different electrocatalysts, the EIS spectra were investigated at an open circuit voltage of 0.65 V. In Fig. 5(d), the CuSe-gCN Nyquist plots are displayed. Installing CuSe and gCN is possible using the comparable circuit. The charge transfer resistance of the composite CuSe-gCN is 1.05 Ω which is much smaller as compared to the pure prepared materials CuSe (1.23 Ω) and gCN (1.57 Ω). In comparison to CuSe and gCN, the CuSe-gCN composite that was initially synthesized had a mesoporous architecture with pore size of 2.36 nm. As a consequence, the charge transfer resistance Rct was decreased, which is advantageous for improving transfer of electron and diffusion at interface of the electrode/electrolyte. The mesoporous structure supports to enhance the amount of accessible catalytic active sites by increasing the internal reaction space and the area of contact among the electrolyte and active materials. The turnover frequency was evaluated in order to examine the electrocatalytic activity of the generated catalyst on an intrinsic level. To assess the electrode kinetics and charge transfer effectiveness, the TOF values of CuSe-gCN, CuSe, and gCN were calculated using the total number of cations present in the reaction solution. When measured at 208 mV overpotential, the as-prepared CuSe-gCN nanocrystals exhibit enhanced electrocatalytic activity with a TOF value of 1.32 s^{-1} compared to CuSe (0.0043 s^{-1}) and gCN (0.005 s^{-1}), etc. Therefore, the rate measurement that resulted in an estimated TOF of 1.32 s^{-1} for this heterogeneous catalyst utilized the exact concentrations of CuSe and gCN present in a particular electrode. It has been well documented in the literature that when the catalysts cycled, oxy-

Table 2. Comparison table of electrocatalytic activity of synthesized materials with already reported materials in basic medium

Sr. No.	Electrocatalyst	Electrolyte	Tafel slope (mV/dec)	Overpotential (mV)	References
1	InSe/g-C_3N_4	1 M KOH	59	206	[63]
2	Co_3Se@GCN	0.1 M KOH	48	147	[64]
3	Ir_2S-gCN	1.0 M KOH	82	276	[65]
4	Gd_2O_3/gCN	1 M KOH	88	281	[66]
5	Co_3S_4/MnS_2	1.0 M KOH	137	265	[67]
6	CuSe/NF	0.1 M KOH	95	297	[68]
7	$NiSe_2$@$CuSe_2$-NF	1.0 M KOH	74	201	[69]
8	CuSe	1 M KOH	89	294	This Work
9	gCN	1 M KOH	122	360	This Work
10	CuSe-gCN	1 M KOH	35	208	This Work

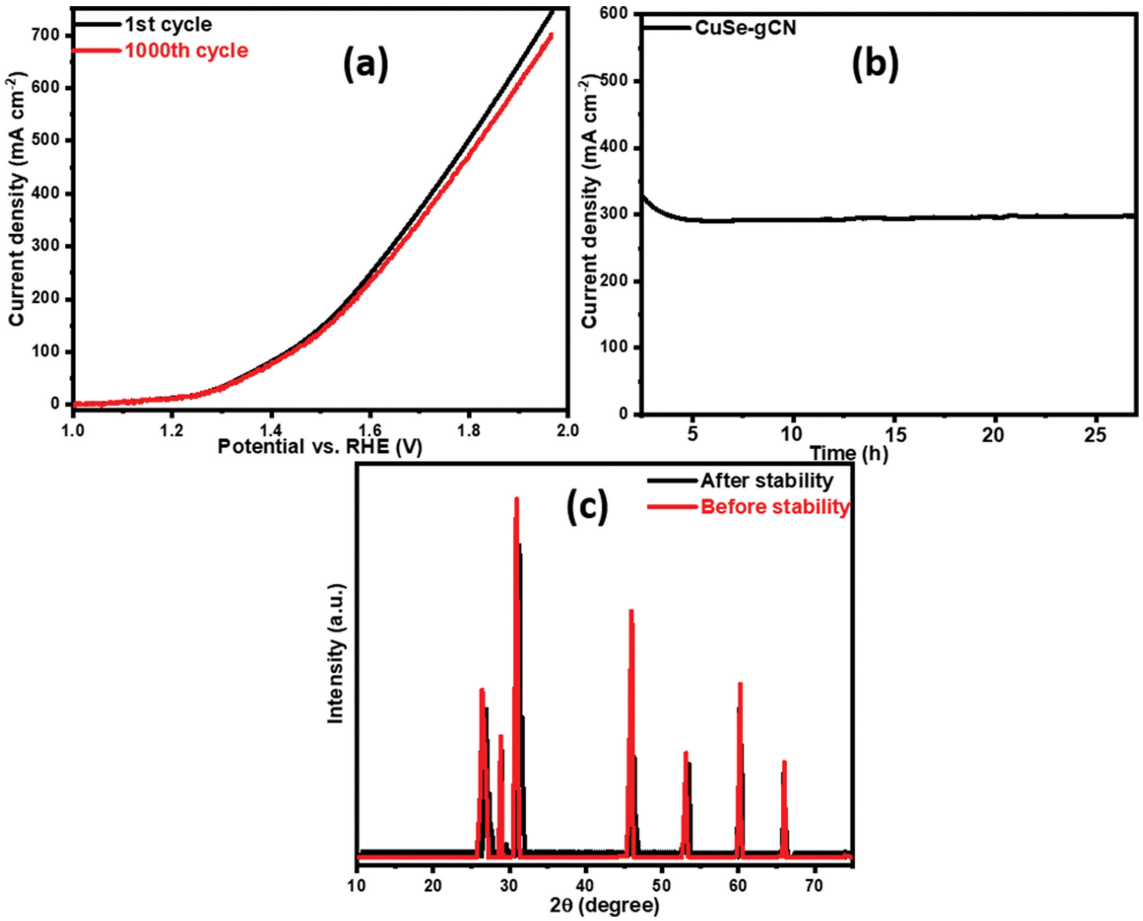

Fig. 6. (a) Comparison of LSV before and after 1000 CV cycles (b) Chronoamperometry test in 1 M KOH solution and (c) XRD pattern before and after stability test.

hydroxide (CuOOH) developed, gradually changing their color from light brown (as such at the time of coating) to black. To increase the number of active sites for OER, cobalt oxy hydrate (CuOOH) has a greater conductivity than CuSe@gCN (see Eqs. (8)-(11)).

$$Cu+OH^- \rightarrow Cu\text{-}OH+e^- \quad (8)$$

$$Cu\text{-}OH+OH^- \rightarrow Cu\text{-}O+H_2O+e^- \quad (9)$$

$$Cu\text{-}O+OH^- \rightarrow Cu\text{-}OOH+e^- \quad (10)$$

$$Cu\text{-}OOH+OH^- \rightarrow Cu+O_2+H_2O+e^- \quad (11)$$

Stability was considered another crucial indicator for the catalyst's potential application by comparing the plots in OER before and after 1000 cycles at 10 mV/s scan rate under a voltage range of 1.2-2.0 V. The CuSe-gCN electrocatalyst displays virtually little modification in the LSV curves before and after 1000 cycles, as revealed in Fig. 6(a), highlighting the OER process' very long lifetime. In Fig. 6, it is depicted that the catalysts for the comparable CuSe-

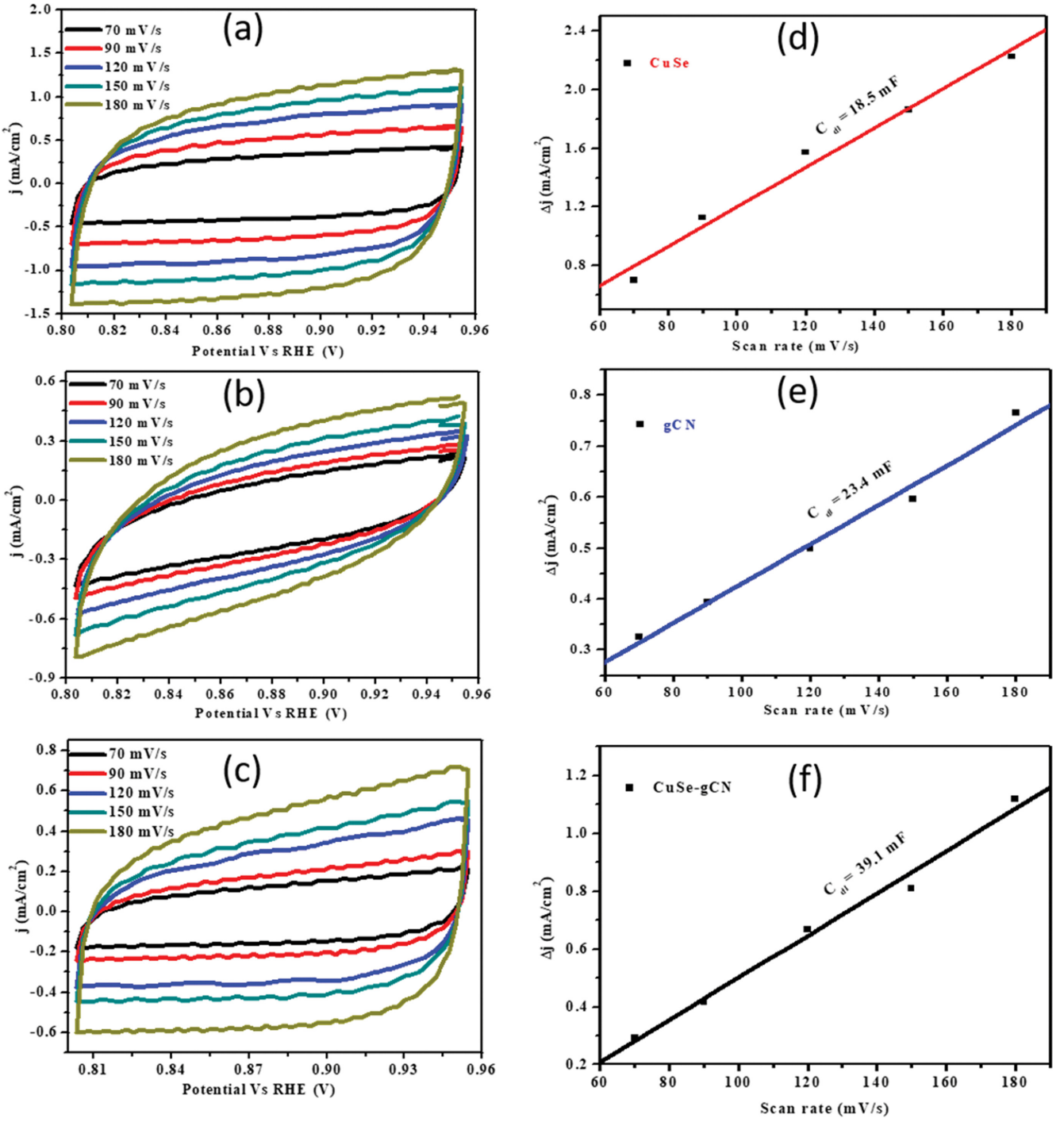

Fig. 7. Comparison table (a)-(c) CV curves of CuSe-gCN, CuSe and gCN at different scan rates in basic media, (d)-(f) respective Cdl values measured through linear fit slope value.

gCN and gCN are a little bit less stable than CuSe-gCN. Another popular stability test is chronopotentiometry. The CuSe-gCN was assessed for 20 hours at a fixed potential of 0.75 V vs. Ag/AgCl. CuSe-gCN, as seen in Fig. 6(b), is further evidence of the material's exceptional stability as it can keep a constant voltage of 1.42 V vs. RHE. The XRD was performed after the stability test and results show negligible change in the peak intensity and position, which confirms the electrocatalyst was stable.

The curves of cyclic voltammetry (CV) of all manufactured samples, analyzed at a scan rate of 70, 90, 120, 150 and 180 mV/s, are depicted in Fig. 7(a)-(c). All of the samples taken from the as-synthesized materials had two different redox peaks on the CV, indicating that all selenides are electroactive. In addition, it is clear from the findings of this cyclic voltammetry that the addition of graphitic carbon nitride to copper selenide causes an increase in the redox peaks' intensity due to the material's increased electroactivity. All

Table 3. Comparison table of ECSA and C_{dl} values of CuSe, gCN and CuSe-gCN in basic media

Sr. no	Material	ECSA (cm^2)	C_{dl} (mF)
1	CuSe	462.5	18.5
2	gCN	585	23.4
3	CuSe-gCN	977.5	39.1

materials' cyclic voltammetry (CV) curve shapes remain steady as the scan rate is raised, suggesting strong cyclic stability and low electrocatalyst resistance. Cdl was also monitored to evaluate the electrochemically active surface areas (ECSA), as shown in Fig. 7(d)-(f), which illustrate the interaction between scan rates and current densities. According to the results, CuSe-gCN had the highest Cdl values (39.1 mF), followed by CuSe (18.5 mF) and gCN (23.4 mF), indicating that CuSe-gCN had the most active exposed sites and the optimum catalytic activity. A large level of exposure is prevalent at exposed active sites, as evidenced by the higher ECSA value for the CuSe-gCN (Table 3). The roughness factor (Rf) of all the synthesized electrodes was calculated using formula $Rf=A_2/A_1$. Here A_1=geometrical surface area of the electrode (0.5 cm^2) and A_2= ECSA of electrode. The calculated Rf for the CuSe, gCN and CuSe-gCN was 925, 1,170, 1,955, respectively. The higher the Rf of the electrode, the higher will be the electrochemical activity of the electrode. Electrocatalysis is a surface averaged process, hence measuring intrinsic activity using surface average performance is accurate.

This improved catalytic performance is due to a number of factors. According to earlier literature, Cu and Se's complementary structural modification functions, which have higher activity throughout the catalytic process, have a synergistic impact that is central to the improved OER bustle in the first place. The material's large specific surface area and porous structure both work to effectively facilitate the full attachment of active centers to the electrolyte. Contrarily, graphitized carbon nitride (gCN) is used to encase CuSe nanoparticles in order to boost their conductivity while also preventing agglomeration. The results demonstrate that the catalytic process is efficient because the current density barely changes.

CONCLUSION

A straightforward hydrothermal technique was used to design CuSe-gCN nanocomposite. All the physical characterizations confirm the phase composition of CuSe, gCN and CuSe-gCN composite, with mesoporous structure with 2.36 nm pore size. Further, the combination of unique morphology nanocrystals with a vertical shape is decorated with numerous nanoparticles facilitating the OER at low onset potential and achieving higher current densities. The CuSe-gCN catalysts have outstanding electrical conductivity and electrocatalytic activity because of their distinct mesoporous structure. To attain a 10 mA/cm^2 current density, a substantially smaller overpotential of 208 mV was needed in comparison to monometallic CuSe of 294 mV and gCN of 360 mV. Additionally, the CuSe-gCN nanocrystals, as-prepared showed a low Tafel slope of 35 mV/dec and exceptional stability of 30 h using chronoamperometry. To generate a unique catalyst dependent on plentiful and noble-metal-free sources on earth, the current work provides a new potential to change the electrical and active features of electrocatalysts for efficient water electrolysis.

ACKNOWLEDGEMENTS

Princess Nourah bint Abdulrahman University Researchers Supporting Project number (PNURSP2023R55), Princess Nourah bint Abdulrahman University, Riyadh, Saudi Arabia.

DECLARATION

Compliance with Ethical Standards

Yes this article compliance with ethical standards of journal.

Competing Interests

There is no conflict of interest by any form for this manuscript.

Conflict of Interest

The authors declare that they have no conflict of interest.

Research Data Policy and Data Availability Statements

The datasets generated during and/or analyzed during the current study are available from the corresponding author on reasonable request.

Author Contributions

All the authors have equal contributions.

REFERENCES

1. R. J. Goodland, H. E. Daly and S. El Serafy, *Environ. Conserv.*, **20**, 297 (1993).
2. P. K. Bose and D. Maji, *Int. J. Hydrog. Energy*, **34**, 4847 (2009).
3. S. O. Oyedepo, *Energy, Sustain. Soc.*, **2**, 1 (2012).
4. H. Cheng and Y. Hu, *Bioresour. Technol.*, **101**, 3816 (2010).
5. M. Patel and A. Kumar, *Renew. Sustain. Energy Rev.*, **58**, 1293 (2016).
6. M. Hassan, Y. Slimani, M. A. Gondal, M. J. Mohamed, S. Guener, M. A. Almessiere, A. M. Surrati, A. Baykal, S. Trukhanov and A. Trukhanov, *Ceram. Int.*, **48**, 24866 (2022)
7. B. Kumar and P. Verma, *Fuel*, **288**, 119622 (2021).
8. H. Choi, S. Surendran, Y. Sim, M. Je, G. Janani, H. Choi, J. K. Kim and U. Sim, *J. Chem. Eng.*, **450**, 137789 (2022).
9. S. Trukhanov, A. Trukhanov, V. Turchenko, A. V. Trukhanov, E. Trukhanova, D. Tishkevich, V. Ivanov, T. Zubar, M. Salem and V. Kostishyn, *Ceram. Int.*, **44**, 290 (2018).
10. D. Vinnik, V. Kokovkin, V. Volchek, V. Zhivulin, P. Abramov, N. Cherkasova, Z. Sun, M. Sayyed, D. Tishkevich and A. Trukhanov, *Mater. Chem. Phys.*, **270**, 124818 (2021).
11. M. S. Habib, O. Asghar, A. Hussain, M. Imran, M. P. Mughal and B. Sarkar, *J. Clean. Prod.*, **278**, 122403 (2021).
12. X. Chen, C. Li, M. Grätzel, R. Kostecki and S. S. Mao, *Chem. Soc. Rev.*, **41**, 7909 (2012).
13. D. Hall and J. I. Scrase, *Biomass and Bioenerg.*, **15**, 357 (1998).
14. P. Ibarra-Gonzalez and B.-G. Rong, *Chin. J. Chem. Eng.*, **27**, 1523 (2019).
15. A. Trukhanov, V. Kostishyn, L. Panina, V. Korovushkin, V. Turch-

enko, P. Thakur, A. Thakur, Y. Yang, D. Vinnik and E. Yakovenko, *J. Alloys Compd.*, **754**, 247 (2018).
16. X. Li, L. Zhao, J. Yu, X. Liu, X. Zhang, H. Liu and W. Zhou, *Nano-Micro Lett.*, **12**, 1 (2020).
17. S. Hernández, V. Cauda, D. Hidalgo, V. F. Rivera, D. Manfredi, A. Chiodoni and F. C. Pirri, *J. Alloys Compd.*, **615**, S530 (2014).
18. J. Wang, X. Yue, Y. Yang, S. Sirisomboonchai, P. Wang, X. Ma, A. Abudula and G. Guan, *J. Alloys Compd.*, **819**, 153346 (2020).
19. L. Zhang, H. Zhao, S. Xu, Q. Liu, T. Li, Y. Luo, S. Gao, X. Shi, A. M. Asiri and X. Sun, *Small Struct.*, **2**, 2000048 (2021).
20. B. Yao, J. Zhang, X. Fan, J. He and Y. Li, *Small*, **15**, 1803746 (2019).
21. S. Surendran, S. C. Jesudass, G. Janani, J. Y. Kim, Y. Lim, J. Park, M. K. Han, I. S. Cho and U. Sim, *Adv. Mater. Technol.*, **8**, 2200572 (2022).
22. T. Trukhanov S. V. Kazakevich and I. S. Balagurov, *J. Magn. Magn. Mater.*, **393**, 253 (2015).
23. M. Zdorovets, A. Kozlovskiy, D. Tishkevich, T. Zubar and A. Trukhanov, *J. Mater. Sci. Mater. Electron.*, **31**, 21142 (2020).
24. M. A. Almessiere, A. V. Trukhanov, Y. Slimani, K. You, S. V. Trukhanov, E. L. Trukhanova, F. Esa, A. Sadaqat, K. Chaudhary and M. Zdorovets, *Nanomater.*, **9**, 202 (2019).
25. T. Wang, L. Tao, X. Zhu, C. Chen, W. Chen, S. Du, Y. Zhou, B. Zhou, D. Wang and C. Xie, *Nat. Catal.*, **5**, 66 (2022).
26. L. Du, Y. Sun and B. You, *Mater. Rep.: Energy*, **1**, 100004 (2021).
27. G. Janani, S. Surendran, H. Choi, T.-Y. An, M.-K. Han, S.-J. Song, W. Park, J. K. Kim and U. Sim, *ACS Sustain. Chem. Eng.*, **10**, 1182 (2021).
28. J. Wang, R. Kong, A. M. Asiri and X. Sun, *ChemElectroChem*, **4**, 481 (2017).
29. S. Surendran, A. Sivanantham, S. Shanmugam, U. Sim and R. Selvan, *Fuel*, **3**, 2435 (2019).
30. S. Park, Y. Shao, J. Liu and Y. Wang, *Energy Environ. Sci.*, **5**, 9331 (2012).
31. R. M. Ramsundar, J. Debgupta, V. K. Pillai and P. A. Joy, *Electrocatalysis*, **6**, 331 (2015).
32. W. Cai, X. Liu, L. Wang and B. Wang, *Mater. Today Nano*, **17**, 100144 (2022).
33. S. Surendran, S. Shanmugapriya, Y. S. Lee, U. Sim and R. Selvan, *ChemistrySelect*, **3**, 12303 (2018).
34. L. H. Zhang, S. Mathew, J. Hessels, J. N. Reek and F. Yu, *ChemSusChem*, **14**, 234 (2021).
35. A. Das, S. C. Mandal, A. S. Nair and B. Pathak, *ACS Phys. Chem. Au*, **2**, 125 (2021).
36. W. Xi, G. Yan, H. Tan, L. Xiao, S. Cheng, S. U. Khan, Y. Wang and Y. Li, *Dalton Trans.*, **47**, 8787 (2018).
37. H. Zhang, W. Tian, X. Duan, H. Sun, S. Liu and S. Wang, *J. Adv. Mater.*, **32**, 1904037 (2020).
38. A. Allangawi, T. Mahmood, K. Ayub and M. A. Gilani, *Mat. Sci. Semicon. Proc.*, **153**, 107164 (2023).
39. J. M. P. Martirez and E. A. Carter, *ACS Catal.*, **10**, 2720 (2020).
40. J. Hu, A. Al-Salihy, J. Wang, X. Li, Y. Fu, Z. Li, X. Han, B. Song and P. Xu, *Adv. Sci.*, **8**, 2103314 (2021).
41. A. Mohajeri and N. L. Dashti, *J. Phys. Chem.*, **123**, 30972 (2019).
42. S. B. Devi, S. Sekar, K. Kowsuki, T. Maiyalagan, V. Preethi, R. Nirmala, S. Lee and R. Navamathavan, *Int. J. Hydrog. Energ.*, **47**, 40349 (2022).
43. R. Gao, H. Zhang and D. Yan, *Nano Energ.*, **31**, 90 (2017).
44. Y. Fan, J. Wang and M. Zhao, *Nanoscale*, **11**, 14836 (2019).
45. N. Kumar, A. Bharti, M. Dixit and A. Nigam, *Powder Metall. Met.*, **59**, 401 (2020).
46. Z. Wang, X. She, Q. Yu, X. Zhu, H. Li and H. Xu, *Energy Fuels*, **35**, 8585 (2021).
47. Y. Liu, S.-C. Yiu, C.-L. Ho and W.-Y. Wong, *Coord. Chem. Rev.*, **375**, 514 (2018).
48. X. Sheng, B. Wouters, T. Breugelmans, A. Hubin, I. F. Vankelecom and P. P. Pescarmona, *ChemElectroChem*, **1**, 1198 (2014).
49. Z. Gu, H. Shen, L. Shang, X. Lv, L. Qian and G. Zheng, *Small Methods*, **2**, 1800121 (2018).
50. X. Xia, L. Wang, N. Sui, V. L. Colvin and W. Y. William, *Nanoscale*, **12**, 12249 (2020).
51. K. Lee, L. Zhang and J. Zhang, *Electrochem. Commun.*, **9**, 1704 (2007).
52. M. Bron, P. Bogdanoff, S. Fiechter, I. Dorbandt, M. Hilgendorff, H. Schulenburg and H. Tributsch, *J. Electroanal. Chem.*, **500**, 510 (2001).
53. G. Li, F. Yin, Z. Lei, X. Zhao, X. He, Z. Li and X. Yu, *Int. J. Hydrog. Energ.*, **47**, 216 (2022).
54. Y. Sun, J. Meng, H. Ju, J. Zhu, Q. Li and Q. Yang, *J. Mater. Chem. A*, **6**, 22526 (2018).
55. I. Chakraborty, N. Ghosh, D. Ghosh, B. Dubey, D. Pradhan and M. Ghangrekar, *Int. J. Hydrog. Energ.*, **45**, 31056 (2020).
56. X. Luo, H. Ma, J. Gao, L. Yu, X. Gu and J. Liu, *Ind. Eng. Chem.*, **61**, 2081 (2022).
57. X. Kong, X. Liu, Y. Zheng, P. K. Chu, Y. Zhang and S. Wu, *Mater. Sci. Eng. Rep.*, **145**, 100610 (2021).
58. X. Li, J. Zhang, L. Shen, Y. Ma, W. Lei, Q. Cui and G. Zou, *Appl. Phys.*, **94**, 387 (2009).
59. B. Pejova and I. Grozdanov, *J. Solid State Chem.*, **158**, 49 (2001).
60. S.-Y. Zhang, C.-X. Fang, Y.-P. Tian, K.-R. Zhu, B.-K. Jin, Y.-H. Shen and J.-X. Yang, *Cryst. Growth Des.*, **6**, 2809 (2006).
61. M. Sajjad, M. Z. U. Shah, M. S. Javed, M. S. Shah, A. Shah, W. Lu and Z. Mao, *J. Energy Storage*, **55**, 105304 (2022).
62. R. Bardestani, G. S. Patience and S. Kaliaguine, *CJCE*, **97**, 2781 (2019).
63. C. He, J. Zhang, W. Zhang and T. Li, *J. Phys. Chem.*, **10**, 3122 (2019).
64. M. Tahir, N. Mahmood, X. Zhang, T. Mahmood, F. Butt, I. Aslam, M. Tanveer, F. Idrees, S. Khalid and I. Shakir, *Nano Res.*, **8**, 3725 (2015).
65. J. Chen, P. Cui, G. Zhao, K. Rui, M. Lao, Y. Chen, X. Zheng, Y. Jiang, H. Pan and S. X. Dou, *Angewandte Chemie.*, **58**, 12540 (2019).
66. S. Chandrasekaran, D. Ma, Y. Ge, L. Deng, C. Bowen, J. Roscow, Y. Zhang, Z. Lin, R. Misra and J. Li, *Nano Energ.*, **77**, 105080 (2020).
67. R. Zhang, Z. Yu, R. Jiang, J. Huang, Y. Hou, F. Yang, H. Zhu, B. Zhang, Y. Huang and B. Ye, *Electrochim. Acta*, **366**, 137438 (2021).
68. B. Chakraborty, R. Beltrán-Suito, V. Hlukhyy, J. Schmidt, P. W. Menezes and M. Driess, *ChemSusChem*, **13**, 3222 (2020).
69. T. Li, Q. Zhang, X. H. Wang, J. Luo, L. Shen, H. C. Fu, F. Gu, N. B. Li and H. Q. Luo, *Nanoscale*, **13**, 17846 (2021).